Nano Energy 79 (2021) 105458

Contents lists available at ScienceDirect

Nano Energy

journal homepage: http://www.elsevier.com/locate/nanoen

On the irreversible sodiation of tin disulfide

Xiuzhen Wang [a,b,c,1], Zhenpeng Yao [d,e,1], Sooyeon Hwang [f], Lei Zhang [g], Maosen Fu [h], Shuang Li [f], Liqiang Mai [g], Qingyu Xu [c,*], Dong Su [b,*]

[a] School of Energy and Power, Jiangsu University of Science and Technology, Zhenjiang 212003, China
[b] National Laboratory for Condensed Matter Physics, Institute of Physics, Chinese Academy of Sciences, Beijing 100190, China
[c] School of Physics, Southeast University, Nanjing 211189, China
[d] Department of Chemistry and Chemical Biology, Harvard University, Cambridge, MA 02138 USA
[e] Department of Chemistry and Department of Computer Science, University of Toronto, Toronto, Ontario M5S 3H6, Canada
[f] Center for Functional Nanomaterials, Brookhaven National Laboratory, Upton, NY 11973, USA
[g] State Key Laboratory of Advanced Technology for Materials Synthesis and Processing, Wuhan University of Technology, Wuhan 430070, China
[h] State Key Laboratory of Solidification Processing, School of Materials Science and Engineering, Northwestern Polytechnical University, Xi'an 710000, China

ARTICLE INFO

Keywords:
Tin disulfide
Sodiation reaction
In situ transmission electron microscopy
Phase transition

ABSTRACT

Tin disulfide is considered as a promising electrode material for sodium-ion batteries because of its two-dimensional layered structural characteristics allowing the intercalation of Na ions. Understanding the underlying reaction mechanisms and the decisive step of the reaction reversibility is critical for its applications. Herein, we investigate the sodiation and desodiation processes of SnS_2 by employing *in situ* transmission electron microscopy (TEM). After the initial intercalation reaction, a rock-salt Na_ySnS_2 phase with disordering Na and Sn cations is observed, followed with a conversion reaction and an alloying reaction. The disordering reaction occurs along < 1–10 > direction of pristine SnS_2 phase which is correlated with local bonding rearrangements induced by the exchange of Sn and Na cations. In-situ TEM studies and first-principles calculations indicate that the original 2D SnS_2 structure could not be recovered during desodiation. Instead, the disordered Na_ySnS_2 phase is finally formed, which indicates that the irreversible disordering transition is the determining step of irreversible cycling. This work probes the structural evolution of sodiation, providing a fundamental understanding of the electrochemical properties of metal sulfides and inspiring rational designs of high performance electrodes for sodium-ion batteries.

1. Introduction

Sodium-ion batteries (SIBs) are considered as the promising alternative to lithium-ion batteries (LIBs) for grid-level energy storage applications due to the low cost and abundance of sodium [1–5]. Lithium and sodium have chemical similarity. However, due to the larger ionic radius (Li^+: 0.76 Å, Na^+: 1.02 Å), different standard reduction potential (Li^+/Li: − 3.04 V, Na^+/Na: − 2.71 V) and electronegativity of sodium ions [6], the sodiation reactions may have different reaction kinetics from the corresponding lithium ones. The performances of state-of-the-art SIBs are still not comparable with LIBs in terms of energy density and cyclability, and the design of the next generation of rechargeable SIBs demands electrode materials with high energy density and fast charging/discharging capability. Two dimensional metal dichalcogenides (MoS_2 [7], TiS_2 [8], WS_2 [9], SnS_2 [10], SeS_2 [11] and TaS_2 [12] et al.) have been investigated as potential electrode candidates for SIBs because of their high theoretical capacity. These sulfides consist of 2D covalent bonded metal-chalcogenide slabs (MX), bound by van der Waals force, where alkali-metal ions can be inserted into [13–17].

SnS_2 has attracted widespread attention as anode for SIBs due to their large interlayer spacing of 0.59 nm which can accommodate sodium ions and a remarkable theoretical capacity of 1136 mAh g^{-1} [18–21]. Recently, Wang et al. synthesized SnS_2/C nanospheres delivering a high initial discharge capacity of 1100 mAh g^{-1} and a reversible capacity of 570 mAh g^{-1} after 100 cycles [22]. Tao et al. reported nitrogen-doped graphene sheet composite (SnS_2/NGS) exhibiting an initial discharge capacity of 1147 mAh g^{-1} and a reversible capacity of

* Corresponding author.
E-mail addresses: xuqingyu@seu.edu.cn (Q. Xu), dongsu@iphy.ac.cn (D. Su).
[1] These authors contributed equally to this work.

https://doi.org/10.1016/j.nanoen.2020.105458
Received 15 August 2020; Received in revised form 1 October 2020; Accepted 3 October 2020
Available online 6 October 2020

453 mAh g^{-1} was maintained after 200 cycles at the current density of 500 mA g^{-1} [23]. The capacity of the porous carbon/tin sulfide aerogel (SSC@SnS_2) reaches 432 mAh g^{-1} after 1000 cycles [24]. Despite those pleasing performances, the large irreversible capacity loss after the first cycle and the poor retention properties for long cycles call for further investigation. These issues can be attributed to two factors: (1) the decomposition of electrolyte to form solid-electrolyte interface (SEI) film at the initial cycle and the instability of SEI during following cycles, which is a general issue for oxide and sulfide based electrodes [25–27]; (2) the irreversible structural changes in SnS_2 nanostructure upon the first sodiation, which is associated with the phase evolution. Up to now, irreversible structural change during sodiation of SnS_2 is still not fully understood, especially because there are several reaction steps which have different reaction natures.

It was proposed that the sodiation in SnS_2 include three steps, firstly an intercalation reaction, followed by conversion reaction, and then alloying reaction, as described in following equations [19,28,29]:

$$x\mathrm{Na} + \mathrm{SnS_2} \rightarrow \mathrm{Na}_x\mathrm{SnS_2} (0 < x < 1) \quad (1)$$

$$(4-x)\mathrm{Na} + \mathrm{Na}_x\mathrm{SnS_2} \rightarrow 2\mathrm{Na_2S} + \mathrm{Sn} \quad (2)$$

$$\mathrm{Sn} + 3.75\mathrm{Na} \rightarrow \mathrm{Na}_{3.75}\mathrm{Sn} \quad (3)$$

Totally up to 7.75 Na can be accommodated by one formula of SnS_2, which corresponds to a capacity of 1136 mAh g^{-1} after the reaction of Eq. (3). These equations were actually deduced from the cyclic voltammetry tests while detailed structural characterization is needed to confirm these reaction equations. *In situ* transmission electron microscopy (TEM) technique offers a powerful tool for directly visualizing the electrochemical reaction processes of electrode at the atomic scale in real time [30–35]. Recent reports using *in situ* TEM technique revealed further information of the sodiation/desodiation of SnS_2. Gao et al. tracked the insertion and extraction of Na ions with high resolution TEM and observed the formation of intermediate superstructure $Na_{0.5}SnS_2$ during de-intercalation process [36]. Ma et al. studied sodiation processes of two SnS_2 structures, trigonal P-3m1 and hexagonal $P6_3mc$ phases, with *in situ* electron diffraction, and found that different $NaSnS_2$ phases (AA1 and AB1) during intercalation reaction process generated the same final phases after being fully discharged [37]. These works provided valuable information for the preliminary understanding of the sodiation process of SnS_2, however, the microscopic and comprehensive insights about the whole sodiation/desodiation reaction, especially on what caused irreversible capacities, still remain elusive. The in-depth investigation on the structural evolution is highly needed in order to develop SnS_2 for SIBs.

In this work, we studied the reaction dynamics of SnS_2 during sodiation and desodiation processes in real-time by *in situ* TEM complemented by first-principles calculations. We revealed a sophisticated reaction pathway in the sodiation processes, in contrast to the previous reports. A disordering reaction occurred with the formation of the rock-salt (Na_ySnS_2) phase. The rearrangement of cations and the change of layered structure were followed by disordering reaction. Subsequent conversion and alloying reactions further destroyed the layered structure. It is worth noting that the sodiated mixture can only be partially oxidized to Na_ySnS_2 (rock-salt) through desodiation reaction. The sodiation reaction is partially reversible, and de-alloying and de-conversion is the dominant reaction mechanism of desodiation. The asymmetric reaction pathways in sodiation/desodiation reactions and significant changes in morphology and structure may shed light on the loss of initial charge capacity and the origins of voltage hysteresis. Our work provides a comprehensive understanding of sodiation and desodiation mechanisms in SnS_2, which is critical to bring benefits to optimize 2D metal sulfide electrodes for SIBs.

2. Materials and methods

2.1. Materials

Tetrachlorostannane pentahydrate ($SnCl_4{\cdot}5H_2O$) and 1.2 g thioacetamide (TAA) were dissolved into 40 mL ethanol. The above solution was transferred into a sealed Teflon-lined autoclave at 180 °C for 24 h. After cooling down, the obtained SnS_2 product were washed with deionized water and then dried at 60 °C for 8 h.

2.2. In situ TEM characterization

The *in situ* TEM experimental setup was incorporated into a Nanofactory TEM-STM specimen holder. SnS_2 nanosheets were dispersed onto a half lacey carbon gold, Na metal was attached to a piezo-driven W probe as the counter electrode, and the thin layer of Na_2O and NaOH formed on the surface of Na metal as solid-state electrolyte to allow transport of sodium ions. SnS_2 sample before and after cycling were stored and processed in an Ar-filled glovebox to avoid the exposure to air. All the *in situ* and *ex situ* TEM measurements were performed on a JEOL 2100 F TEM operated at 200 kV, and supplementary *ex situ* characterization was conducted on a Hitachi HD2700C scanning transmission electron microscope (STEM) operated at 200 kV.

2.3. Electrochemical measurements

The active material electrodes were prepared by casting the slurry containing SnS_2, acetylene black, and polyvinylidene fluoride in a weight ratio of 8:1:1 in *N*-methyl-2-pyrrolidone on a copper foil current collector. Electrochemical measurements were carried out on coin cells. The CR2032-type coin cells were assembled in an Ar-filled glovebox with an SnS_2 electrode as the working electrode, glass microfiber as the separator, pure Na foil as the counter electrode, and 1 M $NaClO_4$ in ethylene carbonate/dimethyl carbonate (EC:DMC = 1:1 in volume) as the electrolyte. An electrochemistry workstation (CHI660b) was utilized to conduct measurements in cyclic voltammetry at 0.1 mV s^{-1}. The galvanostatic charge/discharge tests were performed on a battery test system (NEWARE BTS4000) with a voltage range of 3.0–0.01 V. After the electrochemical tests, the coin cells were disassembled in the Ar-filled glovebox. The cycled electrode materials were washed with DMC several times and then dispersed onto a Cu grid for *ex situ* TEM characterization.

2.4. First-principles calculations

First-principles density functional theory (DFT) calculations reported in this study were conducted using the Vienna Ab initio Simulation Package (VASP) [38–41] within the projector augmented wave (PAW) formalism [42] and we used the Perdew–Becke–Ernzerhof (PBE) approximation to deal with the exchange-correlation potential [43]. vdW-D2 functional was adopted including a self-consistent van der Waals (vdW) correction [44]. A plane wave basis with a cut off energy of 520 eV and **Γ**-centered *k*-meshes with a density of 8000 *k*-points per reciprocal atom were used.

We computed the average sodiation/desodiation voltage (relative to Na/Na^+) using the negative of the reaction free energy per Na added/removed, as shown in Eq. (4):[45].

$$V = \frac{\Delta G_f}{F \Delta N_{Na}} \quad (4)$$

where F is the Faraday constant, ΔN_{Na} is the amount of Na added/removed and ΔG_f is the (molar) change in free energy of the reaction. Considering a two-phase reaction between Na_xMS and Na_yMS: $Na_xMS + (y-x)Na \rightarrow Na_yMS$, ΔG_f can be approximated by the total internal energies from DFT calculations neglecting the entropic

contributions (0 K),

$$\Delta E = E(\mathrm{Na_yMS}) - E(\mathrm{Na_xMS}) - (y-x)E(\mathrm{Na_{metal}}) \quad (5)$$

where $E(\mathrm{Na_xMS})$ and $E(\mathrm{Na_yMS})$ are the DFT total energies at the respective compositions.

3. Results and discussion

The high angle annular dark-field (HAADF)-scanning transmission electron microscopy (STEM) image shows the flower-like SnS_2 samples are composed of thin nanosheets, as shown in Fig. 1a. The electron diffraction patterns and high-resolution transmission electron microscopy (HRTEM) image of the thin SnS_2 nanosheet indicate the

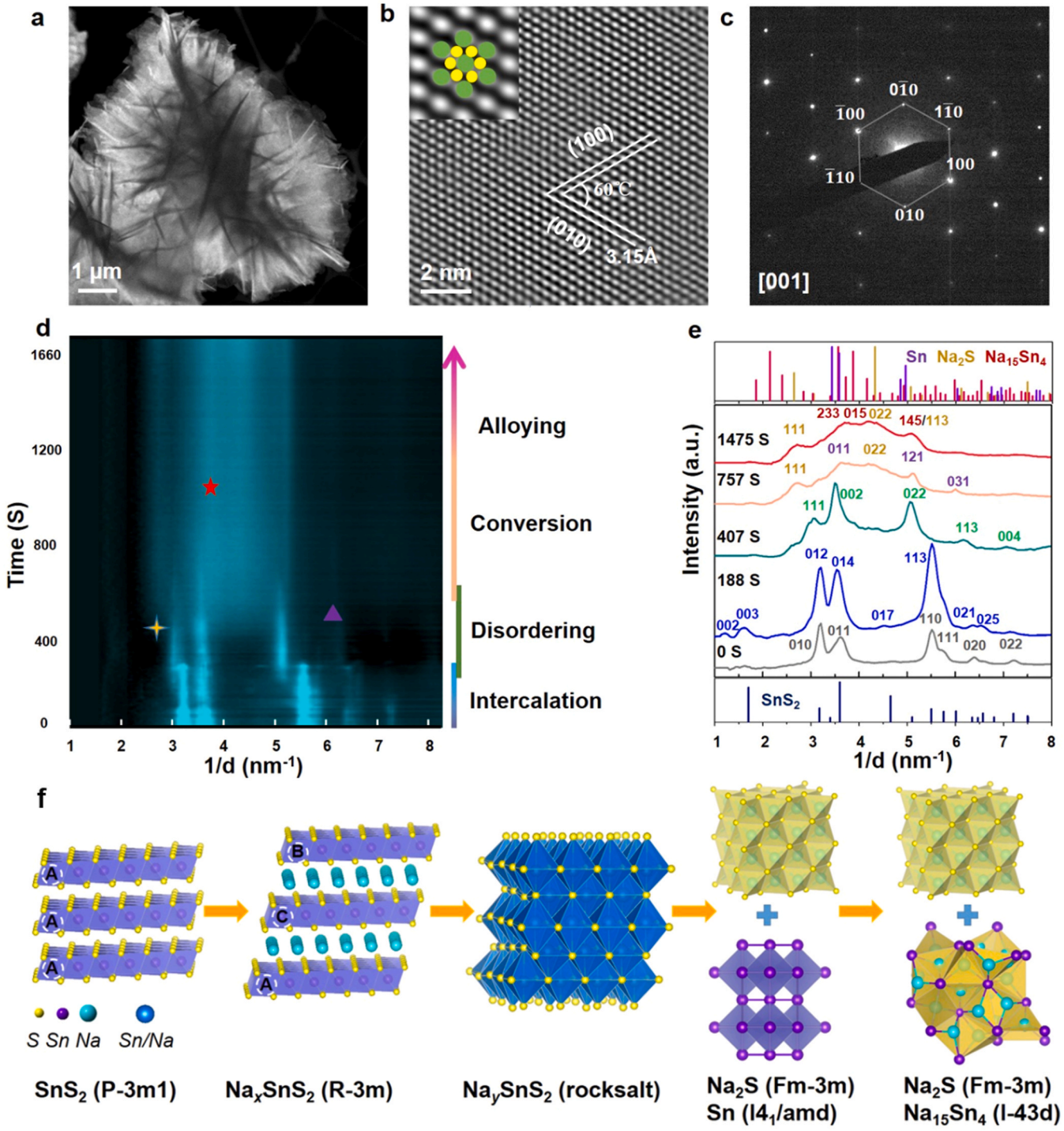

Fig. 1. (a) Low magnification HAADF-STEM image of pristine SnS_2 sample. (b) HRTEM image and (c) SAED pattern of SnS_2 nanosheet seen along [001] zone axis and the atomic model overlapping with enlarged image are shown in the inset. (d) *In situ* electron diffraction intensity profile as a function of reaction time during sodiation of SnS_2. The yellow, purple and red marks indicate the peak of Na_2S, Sn and $Na_{15}Sn_4$, respectively. (e) Corresponding indexed radial intensity profiles of SAED patterns at 0 s, 188 s, 407 s, 757 s, and 1475 s. (f) Atomic models representing intermediate phase evolution during the whole sodiation process, different atoms with different colors. The atoms with dark-blue in the rock-salt phase represent placeholders with equal probability of Na or Sn cations. (For interpretation of the references to colour in this figure legend, the reader is referred to the web version of this article.)

hexagonal-structure along the [001] direction, as shown in Fig. 1b, c. The X-ray diffraction (XRD) pattern (Fig. S1) verifies the pure-phase and well-crystallized layered SnS_2 with P-3m1 space group (JCPDS No. 23-0677). Such nano-scale ultrathin sheet geometry provides an ideal platform for investigating the electrochemical reactions of SnS_2 with sodium by TEM technique and understanding the underlying atomistic mechanism.

To study the phase evolution of SnS_2 during sodiation, *in situ* TEM technique was applied. A series of selected area electron diffraction (SAED) patterns were recorded during sodiation reaction. To directly observe the whole sodiation reaction, radial intensity profiles are plotted as a function of reaction time from a series of real-time SAED patterns, shown in Fig. 1d. Raw video are presented in Movie S1. We extract the raw SAED patterns of the sample during the reaction and find different reaction steps, respectively, shown in Fig. S2. Layered Na_xSnS_2 phase forms as Na ions insert between the Sn-S slabs of the layered SnS_2 under the potentiostatic conditions (− 3.5 V). With further insertion of Na ions, Na_ySnS_2 of face-centered cubic (FCC) structure is observed according to the characteristic FCC diffraction rings appearing at 407 s. In the next step, the patterns confirm the formation of metallic Sn at 757 s and transformation to $Na_{15}Sn_4$ at 1475 s. It is obvious that the peaks disappear or appear as the sodiation progresses in radial intensity profiles (Fig. 1d), verifying the overall phase transformation process. The yellow, purple and red marks indicate the peak of Na_2S, Sn and $Na_{15}Sn_4$, respectively. The overlap of peaks is due to the simultaneous occurrence of several phases in the field of view and the highly inhomogeneous nature of the reaction. The diffraction profiles at 0, 188, 407, 757, and 1475 s are also plotted and indexed in Fig. 1e. In our studies, we have found four steps of sodiation processes of SnS_2: intercalation reaction, disordering reaction, conversion reaction, and alloying reaction. Fig. 1f shows the atomic models of these intermediate phases transition reaction. The initial Na ions intercalation prompt the phase transition from the P-3m1(SnS_2) phase to the R-3m (Na_xSnS_2) phase, in which Na ions occupy the octahedral sites. The insertion of Na ions triggers a sliding of every other S-Sn-S slab in the host structure, the Sn cation layer stacking changes from A-A-A to A-C-B. With further Na ion insertion, the rock-salt (Na_ySnS_2) phase is identified based on the DFT calculations and SAED analysis. Na_ySnS_2 phase has a disordered rock-salt structure, in which the sequence of S anion remains similar to Na_xSnS_2 (R-3m) while Sn and Na cations are disordered. Na and Sn equally occupy the octahedral sites, and the rearrangement of cations completely changes the layered structure, making the Na-intercalation impossible. Excessive Na ions can trigger a conversion reaction with the formation of Na_2S (Fm-3m) and Sn ($I4_1/amd$). No intermediate SnS phase was observed in our *in-situ* TEM experiment indicating that the conversion reaction was accomplished by one-step reaction instead of the two-step reaction in the literature [37]. Finally, Sn metal further reacts with Na to form $Na_{15}Sn_4$ (I-43d) *via* an alloying reaction.

Supplementary material related to this article can be found online at doi:10.1016/j.nanoen.2020.105458.

The morphology changes and reaction dynamics are critical to electrode stability and reversibility during cycling. We monitored the morphological and structural evolution of the SnS_2 nanosheet during entire sodiation progress by *in situ* STEM technique in real space. Fig. 2a presents time-sequence annular dark-field (ADF)-STEM images with false colors to visually distinguish the pristine SnS_2 (purple), intercalated Na_xSnS_2 (blue), disordered Na_ySnS_2 (green), metallic Sn and Na_2S composite (brown) and alloying composite (red). The raw ADF-STEM images and video are shown in Fig. S3 and Movie S2. During the initial reaction, only a slight contrast change was observed from the video. The video was recorded on a single crystalline nanosheet of SnS_2 along [001] zone axis. The nanosheet has {100} facets. During intercalation reaction (up to 320 s), although the phase change can be recognized from the change of bend contours, the phase boundary could not be detected because of the very small lattice changes in *a-b* plane. At 460 s, a clear phase boundary started to propagate from top left to bottom right, corresponding to the phase transition from 2D layered structure (Na_xSnS_2) to disordered rock-salt structure (Na_ySnS_2). During this process, Sn ions initially migrate to the intermediary tetrahedral site of the Na layer and then move to neighboring octahedral sites while Na move to the empty Sn sites, as indicated by the dotted red line with arrows in Fig. 2b [46]. Due to the different bonding lengths of Sn-S (2.752 Å) and Na-S (2.920 Å), the exchange of Sn and Na cations cause the change of the local bonding nature by breaking the 3-fold symmetry (Fig. 2c) which may lead to the disordering reaction preferentially happened along certain directions. Interestingly, strips along $< 1\text{–}10 >$ in Na_xSnS_2 nanosheet were observed at 760 s, which can be possibly caused by the anisotropic stress resulting from the cation exchange. With further Na ions diffusion, a conversion reaction takes place *via* the nucleation of Na_2S and Sn nanoparticles. Finally, the alloy reaction between the Sn metal and Na ions proceeds to form Na-Sn alloy *via* the growth of nanoparticles. Fig. 2e, f shows the enlarged images of the region marked by the squares (named as "S1" and "S2") in Fig. 2a at 1399 s and 3000 s. The propagation of the reaction front and kinetics during sodiation can be studied by tracking the movement of geometrical boundaries as in the time lapse snapshots. We quantified the projected area change of the different phases *versus* the sodiation time in Fig. 2d. The projected prolongation speed of each step of sodiation process is estimated to be 70–470 $nm^2\ s^{-1}$, based on the equation $D = \Delta S/\Delta t$, where D is the projected prolongation speed, ΔS is the change of projected reaction area, and Δt is the reaction time. Our analyses can give an estimation of the reaction kinetics in the solid-state. The corresponding SAED and HRTEM images before and after the *in situ* sodiation are presented in Fig. 2g–i, respectively. The figures show significant changes by comparing the pristine images and sodiated images, which further proved that the final products of the alloy reaction were $Na_{15}Sn_4$ nanoparticles and Na_2S composite. Additionally, low-mag DF images of pristine and sodiated (Fig. S4) show that the in-plane area expansion is about 26.1% after the whole sodiation. From the HAADF images of SnS_2 in sodiated state, as shown in Fig. S5a, Na_2S matrix was observed, while the lacking of $Na_{15}Sn_4$ may be due to the poor crystallinity and sensitivity to electron beams. As seen in Fig. S5b–e, S (red) and Na (blue) elements are uniformly distributed in the sodiated SnS_2 nanosheet, whereas the Sn (green) element is particularly enriched at some nanoparticles, due to $Na_{15}Sn_4$ nanoparticles embedded in the Na_2S buffer layer. The morphological structure evolution and the reaction kinetics of SnS_2 during sodiation are well understood.

Supplementary material related to this article can be found online at doi:10.1016/j.nanoen.2020.105458.

During the desodiation process, the electrochemical phase transformations are crucial for the reversibility and stability of SnS_2 electrode. Therefore, the *in situ* desodiation experiments were performed under higher potential to understand the intrinsic reaction mechanisms in depth. The sodiation is thermodynamically spontaneous, while the desodiation is not a spontaneous reaction and requires higher potential (+ 10 V) and much longer time (3600 s). A radial intensity profile of diffraction patterns in the desodiation process is displayed in Fig. 3a. Raw video is available in Movie S3. Selected diffraction patterns with false colors and the indexed diffraction profiles in time series at 0, 4440 and 5040 s are presented in Fig. 3b. The Sn phase and Na_2S can be identified during the desodiation process. With the further Na extraction, the peaks of Na_2S phase gradually disappear, the characteristic peaks of rock-salt structure are more and more obvious, which should be the Na_ySnS_2 (rock-salt) phase. Although the diffraction pattern of Na_ySnS_2 (rock-salt) is very close to that of SnS (rock-salt) (Fig. S6), based on the disappearance of Na_2S phase, the Na_ySnS_2 (rock-salt) phase should be the main component. The rest of the Sn may take longer time to react due to the sluggish desodiation reaction kinetics. The above *in situ* experimental results indicate that most of the sodiated mixture can only transform back to Na_ySnS_2 (rock-salt) after desodiation and SnS_2 cannot be recovered due to the difficulty of re-ordering of cations. As demonstrated in Fig. 3c, with the extraction of Na, the $Na_{15}Sn_4$ phase

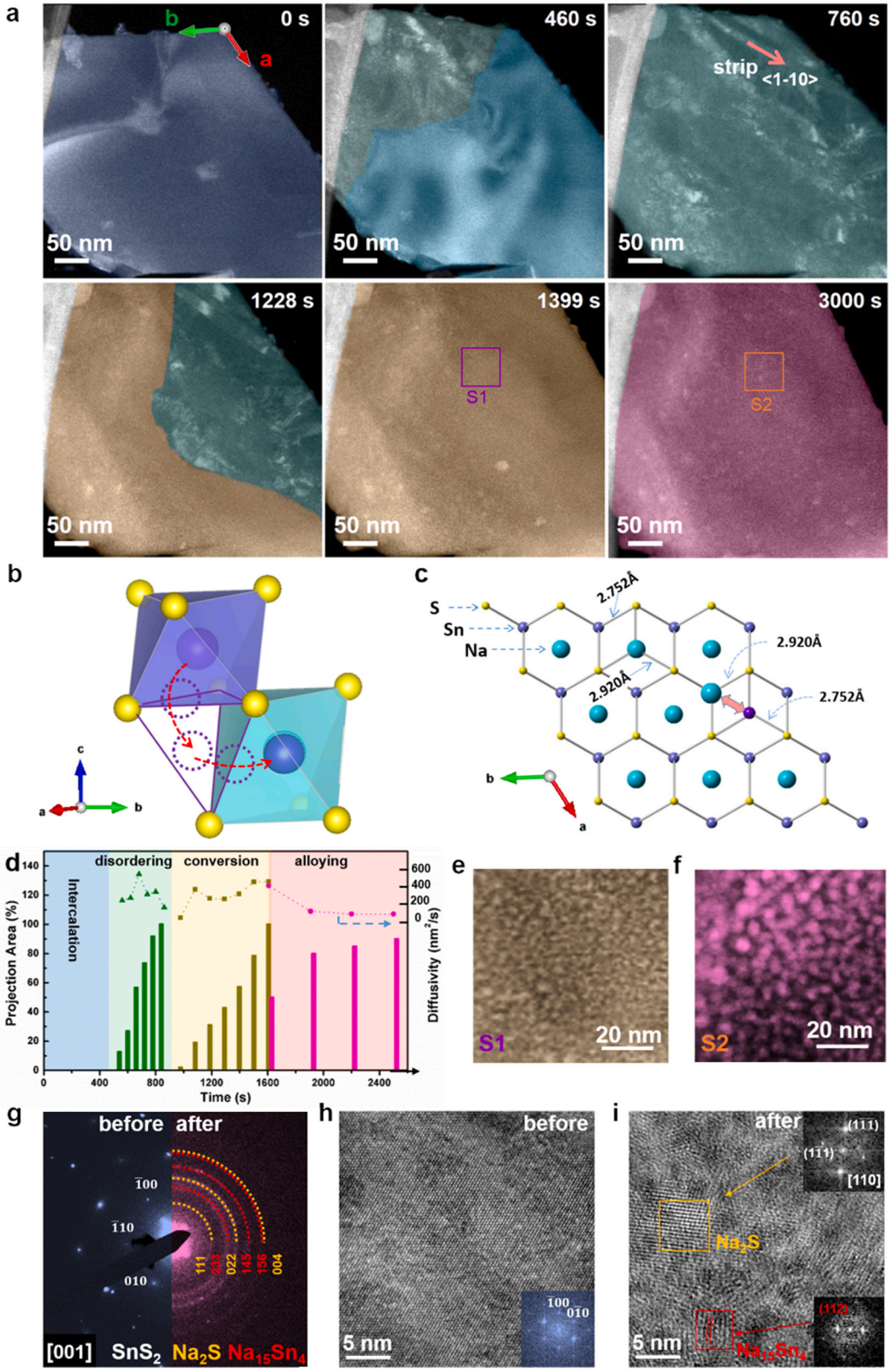

Fig. 2. (a) *In situ* time-sequent dark field STEM images directly show the movement of the phase boundary during multi-step sodiation reaction. The overlaid false colors indicate three different phases: pristine SnS_2 (purple), Na_xSnS_2 (blue), Na_ySnS_2 (green), Sn + Na_2S (brown) and $Na_{15}Sn_4$ + Na_2S (red). (b) Schematic model of the migration path from Sn to Na sites in Na_xSnS_2, and (c) the corresponding atomic model of a Na_xSnS_2 nanosheet. (d) The evolution of projected area of each intermediate phase as a function of sodiation reaction time. (e, f) Enlarged figures of area S1and S2. (g–i) The SAED and HRTEM images before (h) and after (i) *in situ* sodiation (Fig. 2a), respectively. (For interpretation of the references to colour in this figure legend, the reader is referred to the web version of this article.)

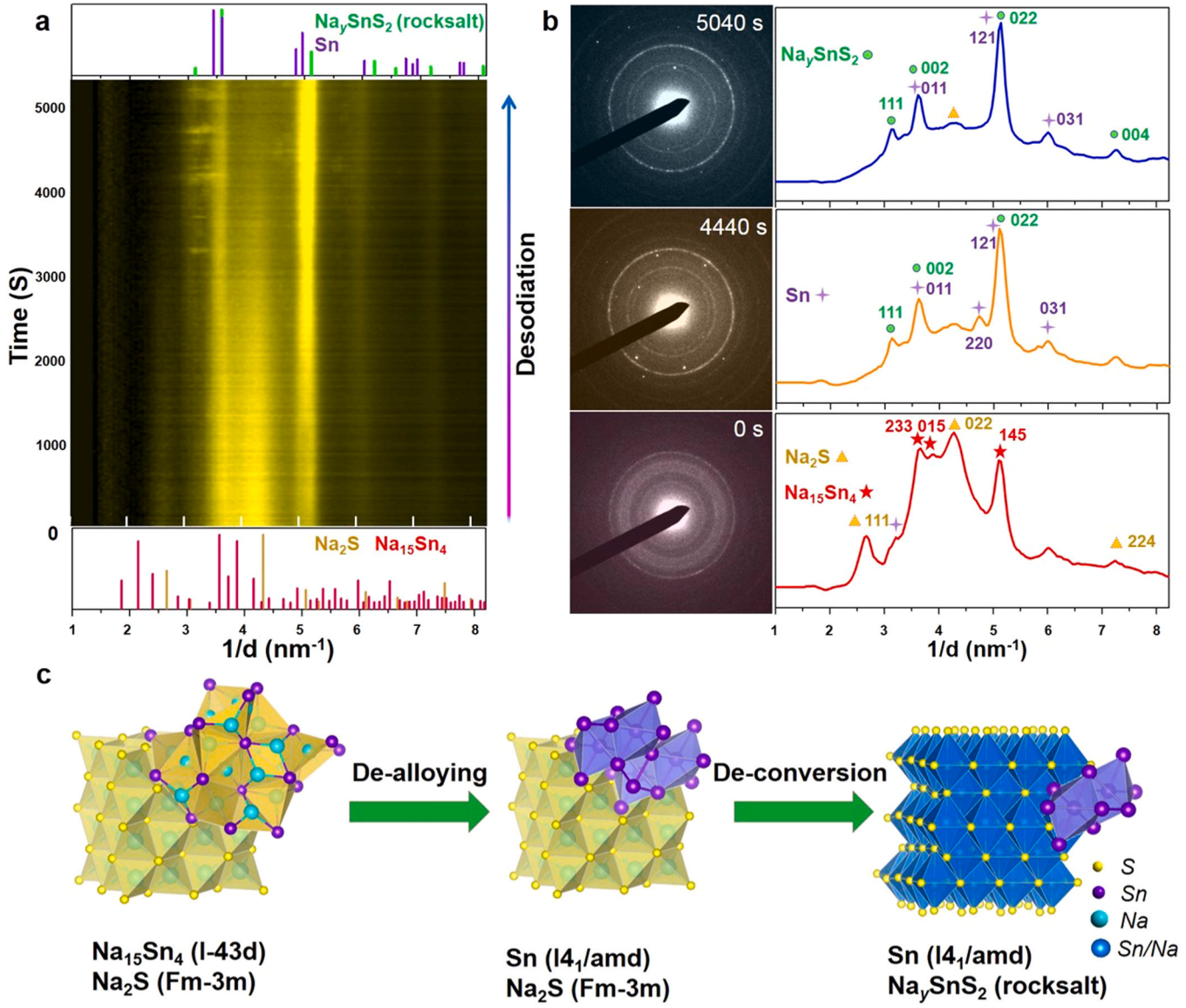

Fig. 3. *In situ* SAED of SnS_2 during desodiation. (a) Electron diffraction intensity profile as a function of reaction time during desodiation process. (b) Selected electron diffraction patterns and indexed radial intensity profiles of diffraction patterns at 0 s, 4440 s and 5040 s. (c) Atomic models representing the phase evolution during the desodiation process.

finally transformed to the Na_ySnS_2 (rock-salt) phase. De-alloying and de-conversion are the dominant reaction mechanism of desodiation. In addition, the reaction processes could be also disclosed by the cyclic voltammetric (CV) curves of SnS_2 electrode at 0.1 mV s^{-1} in Fig. 4a. The cyclic reaction process is consistent with the reaction observed by *in situ* SAED (more details can be obtained from the SI). The irreversibility of cation rearrangement after disordering and the huge structural changes caused by conversion and alloying reaction lead to the poor electrochemical reversibility and sluggish desodiation reaction kinetics.

Supplementary material related to this article can be found online at doi:10.1016/j.nanoen.2020.105458.

In order to verify the consistency of the electrochemical reaction of SnS_2 in coin cell and the reaction process observed in TEM dry-format open cell setup, *ex situ* TEM characterization was also applied in this work. Fig. 4b presents the galvanostatic discharge-charge voltage curves of the SnS_2 electrode at a constant current density of 0.15A g^{-1}. The initial discharge capacity reaches 1276 mAh g^{-1} after the discharge to 0.01 V (theoretical capacity is 1136 mAh g^{-1}). Part of the capacity should be contributed by the formation of the solid-electrolyte interface (SEI) film [47]. The *ex situ* SAED patterns of electrode materials (coin cell) at pristine (Fig. 4c), and discharged (0.01 V) states (Fig. 4d) demonstrate that the sodiation of SnS_2 results in the formation of $Na_{15}Sn_4$ and Na_2S phases. The Na_2S and $Na_{15}Sn_4$ are also confirmed by the *ex situ* HRTEM image and fast-Fourier transform (FFT) patterns, shown in Fig. S7. The *ex situ* TEM results are consistent with the *in situ* results. When charged to 3.0 V, the reversible capacity is about 510 mAh g^{-1} in the first cycle. The initial charge capacity is lower than the first discharge capacity, which limits the advantages of inherent high capacity performance [24,48,49]. *Ex situ* SAED pattern (Fig. 4e) and HRTEM image of the charge electrode (3.0 V) show the formation of Sn and Na_ySnS_2 phase, and STEM-electron energy-loss spectroscopy (EELS) mappings indicate a uniform distribution of Sn and S elements (Fig. S8). Combined with the above *in situ* experiment results, we know that the loss of reversible capacity after the first charge is not only due to the formation of irreversible SEI film, but also the partially reversibility of de-sodiation reaction.

To further investigate the structural evolution during the sodiation/desodiation process of SnS_2, we examine the equilibrium and

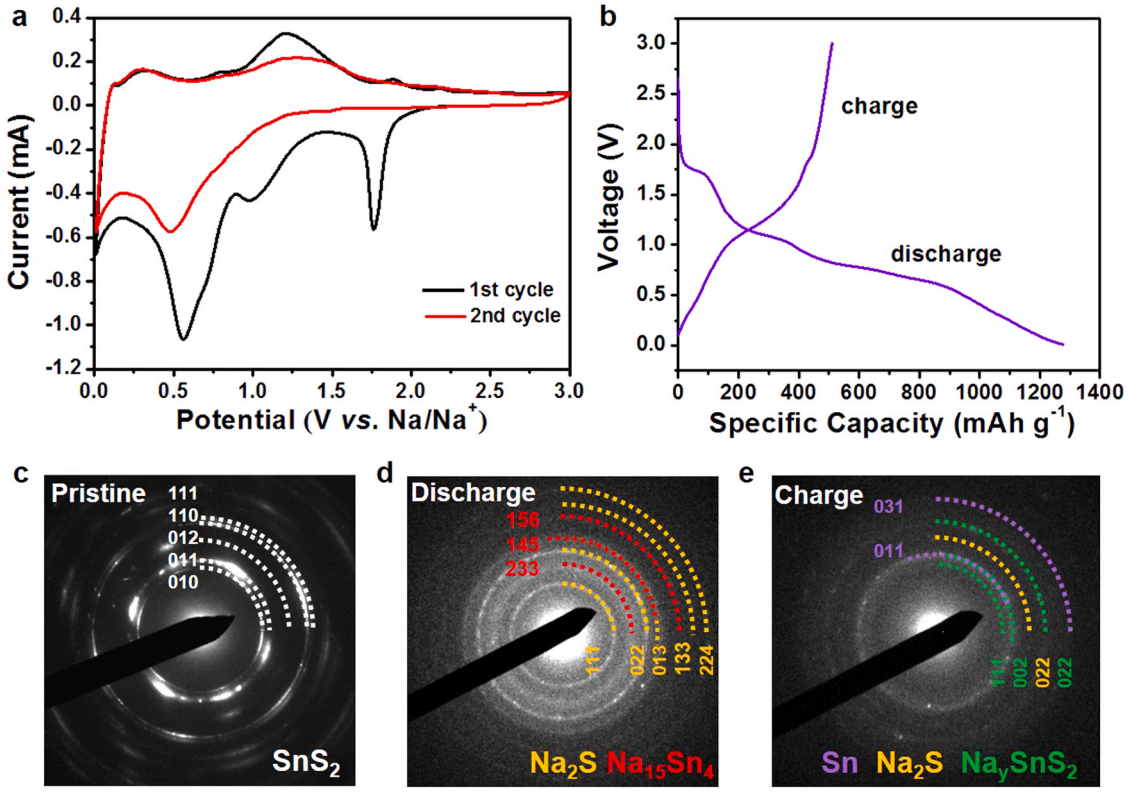

Fig. 4. (a) The cyclic voltammetric (CV) curves of the SnS_2 electrode at 0.1 mV s^{-1}. (b) Galvanostatic discharge-charge curves of the SnS_2 coin cell between 3.0 and 0.01 V. SAED patterns of (c) pristine SnS_2, (d) after discharging to 0.01 V and (e) after charging to 3.0 V.

nonequilibrium reaction pathways through searching the stable intercalated layered phases of Na_xSnS_2 ($0 < x < 3$) using the previous approach [37,50]. We were able to identify two intercalated phases at $x = 1/4$ and $x = 1$, as shown in Fig. 5a, while extensive sodiation will lead to the initiation of conversion reaction. Meanwhile, our experimental observations suggest the existence of disordered rock-salt structured $NaSnS_2$ while it is known that another $NaSnS_2$ (R-3m) exists. For comparison, we build the crystal structure of the disordered rock-salt phase (using the special quasirandom structures method) [51] and R-3m phase, and compare their total energy per f.u. with the intercalated phase ($x = 1$) as identified. The disordered rock-salt phase of $NaSnS_2$ is confirmed with the lowest total energy (Fig. 5a), confirming the existence of a disordering reaction process ($1/4 < x < 1$) following the initial intercalation process ($0 < x < 1/4$) before the conversion step. For the next step, a conversion reaction directly processes to Sn and Na_2S ($1 < x < 4$). Then the sodiation continues through an alloying reaction ($4 < x < 31/4$) with the final products of $Na_{15}Sn_4$ and Na_2S. The calculated sodiation profile shows an agreement with the experimentally measured voltage curve whereas the SnS intermediate phase is not observed by *in situ* experiment (Fig. 5b). The desodiation process proceeds in an equilibrium process, which is through de-alloying reaction to Sn and Na_2S, and reversal conversion reaction to rock-salt Na_ySnS_2. The determined voltage profile also exhibits reasonable agreement with the charge voltage curve, confirming the equilibrium desodiation reaction pathway.

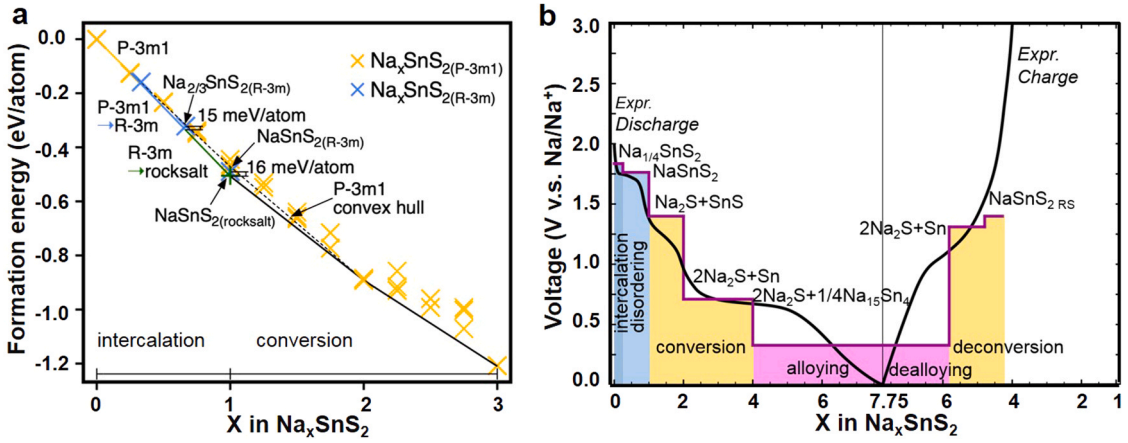

Fig. 5. (a) DFT simulated the sodiation process in SnS_2 crystals and convex hull generated with the calculated nonequilibrium phases of Na-SnS_2. (b) Discharge-charge voltage profiles as a function of Na content in Na_xSnS_2 calculated from first-principles calculation.

4. Conclusions

In summary, we have investigated the phase evolution during sodiation/desodiation processes of SnS_2 nanoflake in real time. Our *in situ* SAED and STEM imaging results combined DFT calculation elucidate four steps of sodiation reaction: intercalation, disordering, conversion and alloying. The disordered cations of Sn and Na restrict the local lattice arrangement and make the reaction preferring along < 1–10 > of Na_xSnS_2 structure. The disordered structure blocks the diffusion channels of layered structure and further sodiaiton triggers conversion reaction and then alloying reaction. It is found that during desodiation, a disordered rock-salt phase (Na_ySnS_2) is reconstituted *via* de-conversion reaction, but the layered structure cannot be recovered, which acts as the limit step of desodiation. This work shows that the reaction nature of SnS_2 is the intrinsic factor determining its overall reaction kinetics and highlights the fundamental mechanism understanding for designing layered sulfide compounds for sodium batteries.

CRediT authorship contribution statement

Xiuzhen Wang: Conceptualization, Investigation, Writing - original draft, Writing - review & editing. **Zhenpeng Yao**: Conceptualization, Writing - original draft, Writing - review & editing. **Sooyeon Hwang**: Investigation, Writing - review & editing. **Lei Zhang**: Resources. **Maosen Fu**: Investigation, Writing - review & editing. **Shuang Li**: Investigation. **Liqiang Mai**: Conceptualization, Resources, Writing - review & editing. **Qingyu Xu**: Conceptualization, Resources, Writing - review & editing, Supervision. **Dong Su**: Conceptualization, Resources, Investigation, Writing - original draft, Writing - review & editing, Supervision.

Declaration of Competing Interest

The authors declare that they have no known competing financial interests or personal relationships that could have appeared to influence the work reported in this paper.

Acknowledgment

This work is supported by the National Natural Science Foundation of China [grant numbers 51771053, 51471085]; the US Department of Energy, Office of Science - Chicago under Award Number [grant number DE-SC0019300]; the National Key Research and Development Program of China [grant number 2016YFA0300803]; the Fundamental Research Funds for the Central Universities, and the open research fund of Key Laboratory of MEMS of Ministry of Education, Southeast University. Dong Su acknowledges the support from the Strategic Priority Research Program (B) [grant number XDB07030200] of Chinese Academy of Sciences. Electron microscopy work was performed at the Center for Functional Nanomaterials, Brookhaven National Laboratory, which is supported by the U.S. Department of Energy (DOE), Office of Basic Energy Science, under contract DE-SC0012704.

Appendix A. Supporting information

Supplementary data associated with this article can be found in the online version at doi:10.1016/j.nanoen.2020.105458.

References

[1] V. Palomares, P. Serras, I. Villaluenga, K.B. Hueso, J. Carretero-González, T. Rojo, Na-ion batteries, recent advances and present challenges to become low cost energy storage systems, Energy Environ. Sci. 5 (2012) 5884.
[2] X. Zheng, C. Bommier, W. Luo, L. Jiang, Y. Hao, Y. Huang, Sodium metal anodes for room-temperature sodium-ion batteries: applications, challenges and solutions, Energy Storage Mater. 16 (2019) 6–23.
[3] C. Zhang, A. Wang, J. Zhang, X. Guan, W.J. Luo, 2D materials for lithium/sodium metal anodes, Adv. Energy Mater. 8 (2018), 1802833.
[4] T. Zhang, Y. Feng, J. Zhang, C. He, D.M. Itkis, J. Song, Ultrahigh-rate sodium-ion battery anode enabled by vertically aligned (1T–2H MoS_2)/CoS_2 hetero-nanosheets, Mater. Today Nano 12 (2020), 100089.
[5] S.W. Kim, D.H. Seo, X. Ma, G. Ceder, K. Kang, Electrode materials for rechargeable sodium-ion batteries: potential alternatives to current lithium-ion batteries, Adv. Energy Mater. 2 (2012) 710–721.
[6] N. Yabuuchi, K. Kubota, M. Dahbi, S. Komaba, Research development on sodium-ion batteries, Chem. Rev. 114 (2014) 11636–11682.
[7] L. David, R. Bhandavat, G. Singh, MoS_2/graphene composite paper for sodium-ion battery electrodes, ACS Nano 8 (2014) 1759–1770.
[8] X. Wang, Z. Yao, S. Hwang, Y. Pan, H. Dong, M. Fu, N. Li, K. Sun, H. Gan, Y. Yao, A. Aspuru-Guzik, Q. Xu, D. Su, In situ electron microscopy investigation of sodiation of titanium disulfide nanoflakes, ACS Nano 13 (2019) 9421–9430.
[9] X. Wang, J. Huang, J. Li, L. Cao, W. Hao, Z. Xu, Improved Na storage performance with the involvement of nitrogen-doped conductive carbon into WS_2 nanosheets, ACS Appl. Mater. Interfaces 8 (2016) 23899–23908.
[10] S. Hwang, Z. Yao, L. Zhang, M. Fu, K. He, L. Mai, C. Wolverton, D. Su, Multistep lithiation of tin sulfide: an investigation using in situ electron microscopy, ACS Nano 12 (2018) 3638–3645.
[11] Q. Li, Y. Xu, Z. Yao, J. Kang, X. Liu, C. Wolverton, M.C. Hersam, J. Wu, V.P. Dravid, Revealing the effects of electrode crystallographic orientation on battery electrochemistry via the anisotropic lithiation and sodiation of ReS_2, ACS Nano 12 (2018) 7875–7882.
[12] J. Wu, J. Peng, Z. Yu, Y. Zhou, Y. Guo, Z. Li, Y. Lin, K. Ruan, C. Wu, Y. Xie, Acid-assisted exfoliation toward metallic sub-nanopore TaS_2 monolayer with high volumetric capacitance, J. Am. Chem. Soc. 140 (2018) 493–498.
[13] M. Fu, Z. Yao, X. Ma, H. Dong, K. Sun, S. Hwang, E. Hu, H. Gan, Y. Yao, E.A. Stach, C. Wolverton, D. Su, Expanded lithiation of titanium disulfide: reaction kinetics of multi-step conversion reaction, Nano Energy 63 (2019), 103882.
[14] Y. Jiang, D. Song, J. Wu, Z. Wang, S. Huang, Y. Xu, Z. Chen, B. Zhao, J. Zhang, Sandwich-like SnS_2/graphene/SnS_2 with expanded interlayer distance as high-rate lithium/sodium-ion battery anode materials, ACS Nano 13 (2019) 9100–9111.
[15] A. Tedstone, D.J. Lewis, P. O'Brien, Synthesis, properties, and applications of transition metal-doped layered transition metal dichalcogenides, Chem. Mater. 28 (2016) 1965–1974.
[16] D. Bin, S. Duan, X. Lin, L. Liu, Y. Liu, Y. Xu, Y. Sun, X. Tao, A. Cao, L. Wan, Structural engineering of SnS_2/graphene nanocomposite for high-performance K-ion battery anode, Nano Energy 60 (2019) 912–918.
[17] Q.H. Wang, K. Kalantar-Zadeh, A. Kis, J.N. Coleman, M.S. Strano, Electronics and optoelectronics of two-dimensional transition metal dichalcogenides, Nat. Nanotechnol. 7 (2012) 699–712.
[18] S. Li, Z. Zhao, C. Li, Z. Liu, D. Li, SnS_2@C hollow nanospheres with robust structural stability as high-performance anodes for sodium ion batteries, Nano-Micro Lett. 11 (2019) 14.
[19] X. Xie, D. Su, S. Chen, J. Zhang, S. Dou, G. Wang, SnS_2 nanoplatelet@graphene nanocomposites as high-capacity anode materials for sodium-ion batteries, Chem. Asian J. 9 (2014) 1611–1617.
[20] Y. Wang, J. Zhou, J. Wu, F. Chen, P. Li, N. Han, W. Huang, Y. Liu, H. Ye, F. Zhao, Y. Li, Engineering SnS_2 nanosheet assemblies for enhanced electrochemical lithium and sodium ion storage, J. Mater. Chem. A 5 (2017) 25618–25624.
[21] B. Qu, C. Ma, G. Ji, C. Xu, J. Xu, Y.S. Meng, T. Wang, J.Y. Lee, Layered SnS_2-reduced graphene oxide composite - a high-capacity, high-rate, and long-cycle life sodium-ion battery anode material, Adv. Mater. 26 (2014) 3854–3859.
[22] J. Wang, C. Luo, J. Mao, Y. Zhu, X. Fan, T. Gao, A.C. Mignerey, C. Wang, Solid-state fabrication of SnS_2/C nanospheres for high-performance sodium ion battery anode, ACS Appl. Mater. Interfaces 7 (2015) 11476–11481.
[23] S. Tao, D. Wu, S. Chen, B. Qian, W. Chu, L. Song, A versatile strategy for ultrathin SnS_2 nanosheets confined in a N-noped graphene sheet composite for high performance lithium and sodium-ion batteries, Chem. Commun. 54 (2018) 8379–8382.
[24] Z. Yang, P. Zhang, J. Wang, Y. Yan, Y. Yu, Q. Wang, M. Liu, Hierarchical carbon@SnS_2 aerogel with "skeleton/skin" architectures as a high-capacity, high-rate capability and long cycle life anode for sodium ion storage, ACS Appl. Mater. Interfaces 10 (2018) 37434–37444.
[25] D. Li, Q. Sun, Y. Zhang, L. Chen, Z. Wang, Z. Liang, P. Si, L. Ci, Surface-confined SnS_2 @C@rGO as high-performance anode materials for sodium- and potassium-ion batteries, ChemSusChem 12 (2019) 2689–2700.
[26] R. Demir-Cakan, Y.S. Hu, M. Antonietti, J. Maier, M.M. Titirici, Facile one-pot synthesis of mesoporous SnO_2 microspheres via nanoparticles assembly and lithium storage properties, Chem. Mater. 20 (2008) 1227–1229.
[27] J. Liang, X.Y. Yu, H. Zhou, H.B. Wu, S. Ding, X.W. Lou, Bowl-like SnO_2 @carbon hollow particles as an advanced anode material for lithium-ion batteries, Angew. Chem. Int. Ed. 53 (2014) 1–6.
[28] L. Fan, X. Li, X. Song, N. Hu, D. Xiong, A. Koo, X. Sun, Promising dual-doped graphene aerogel/SnS_2 nanocrystal building high performance sodium ion batteries, ACS Appl. Mater. Interfaces 10 (2018) 2637–2648.
[29] Y. Liu, H. Kang, L. Jiao, C. Chen, K. Cao, Y. Wang, H. Yuan, Exfoliated-SnS_2 restacked on graphene as a high-capacity, high-rate, and long-cycle life anode for sodium ion batteries, Nanoscale 7 (2015) 1325–1332.
[30] J. Li, G. Johnson, S. Zhang, D. Su, In situ transmission electron microscopy for energy applications, Joule 3 (2019) 4–8.
[31] C.M. Wang, In situ transmission electron microscopy and spectroscopy studies of rechargeable batteries under dynamic operating conditions: a retrospective and perspective view, J. Mater. Res. 30 (2014) 326–339.

[32] K. He, F. Lin, Y. Zhu, X. Yu, J. Li, R. Lin, D. Nordlund, T.C. Weng, R.M. Richards, X. Q. Yang, M.M. Doeff, E.A. Stach, Y. Mo, H.L. Xin, D. Su, Sodiation kinetics of metal oxide conversion electrodes: a comparative study with lithiation, Nano Lett. 15 (2015) 5755–5763.
[33] Z. Fan, L. Zhang, D. Baumann, L. Mei, Y. Yao, X. Duan, Y. Shi, J. Huang, Y. Huang, X. Duan, In situ transmission electron microscopy for energy materials and devices, Adv. Mater. 31 (2019), 1900608.
[34] S. Hwang, D. Su, TEM studies on electrode materials for secondary ion batteries. Encyclopedia of Inorganic and Bioinorganic Chemistry, John Wiley & Sons, Ltd, US, 2019, pp. 1–27.
[35] Y. Huang, C. Zhu, S. Zhang, X. Hu, K. Zhang, W. Zhou, S. Guo, F. Xu, H. Zeng, Ultrathin bismuth nanosheets for stable na-ion batteries: clarification of structure and phase transition by in situ observation, Nano Lett. 19 (2019) 1118–1123.
[36] P. Gao, Y.Y. Zhang, L. Wang, S. Chen, Y. Huang, X. Ma, K. Liu, D. Yu, In situ atomic-scale observation of reversible sodium ions migration in layered metal dichalcogenide SnS_2 Nanostructures, Nano Energy 32 (2017) 302–309.
[37] Z. Ma, Z. Yao, Y. Cheng, X. Zhang, B. Guo, Y. Lyu, P. Wang, Q. Li, H. Wang, A. Nie, A. Aspuru-Guzik, All roads lead to rome: sodiation of different-stacked SnS_2, Nano Energy 67 (2020), 104276.
[38] G. Kresse, J. Furthmüller, Efficiency of ab-initio total energy calculations for metals and semiconductors using a plane-wave basis set, Comput. Mater. Sci. 6 (1996) 15–50.
[39] G. Kresse, J. Furthmüller, Efficient iterative schemes for ab initio total-energy calculations using a plane-wave basis set, Phys. Rev. B 54 (1996) 11169–11186.
[40] G. Kresse, J. Hafner, Ab initio molecular dynamics for liquid metals, Phys. Rev. B 47 (1993) 558–561.
[41] G. Kresse, J. Hafner, Ab initio molecular-dynamics simulation of the liquid-metal-amorphous-semiconductor transition in germanium, Phys. Rev. B 49 (1994) 14251–14269.
[42] P.E. Blöchl, Projector augmented-wave method, Phys. Rev. B 50 (1994) 17953–17979.
[43] J.P. Perdew, M. Ernzerhof, K. Burke, Rationale for mixing exact exchange with density functional approximations, J. Chem. Phys. 105 (1996) 9982–9985.
[44] H. Peelaers, C.G. Van de Walle, First-principles study of van der waals interactions in MoS_2 and MoO_3, J. Phys. Condens. Matter 26 (2014) 305502–305508.
[45] M.K. Aydinol, A.F. Kohan, G. Ceder, K. Cho, J. Joannopoulos, Ab initio study of lithium intercalation in metal oxides and metal dichalcogenides, Phys. Rev. B. 56 (1997) 1354–1365.
[46] D. Eum, B. Kim, S.J. Kim, H. Park, J. Wu, S. Cho, G. Yoon, M. Lee, S. Jung, W. Yang, Voltage decay and redox asymmetry mitigation by reversible cation migration in lithium-rich layered oxide electrodes, Nat. Mater. 19 (2020) 419–427.
[47] Y. Zhang, P. Zhu, L. Huang, J. Xie, S. Zhang, G. Cao, X. Zhao, Few-layered SnS_2 on few-layered reduced graphene oxide as na-ion battery anode with ultralong cycle life and superior rate capability, Adv. Funct. Mater. 25 (2015) 481–489.
[48] L. Wang, Q. Zhao, Z. Wang, Y. Wu, X. Ma, Y. Zhu, C. Cao, Cobalt-doping SnS_2 nanosheets towards high-performance anodes for sodiumion batteries, Nanoscale 12 (2020) 248–255.
[49] Y. Jiang, M. Wei, J. Feng, Y. Ma, S. Xiong, Enhancing the cycling stability of Na-ion batteries by bonding SnS_2 ultrafine nanocrystals on amino-functionalized graphene hybrid nanosheets, Energy Environ. Sci. 9 (2016) 1430–1438.
[50] Z. Yao, S. Kim, J. He, V. Hegde, C. Wolverton, Interplay of cation and anion redox in Li4Mn2O5 cathode material and prediction of improved Li4(Mn,M)2O5 electrodes for Li-ion batteries, Sci. Adv. 4 (2018), eaao6754.
[51] A. Zunger, S. Wei, L.G. Ferreira, J.E. Bernard, Special quasirandom structures, Phys. Rev. Lett. 65 (1990) 353–356.